ACS Energy LETTERS

http://pubs.acs.org/journal/aelccp

VIEWPOINT

# Apparent Defect Densities in Halide Perovskite Thin Films and Single Crystals

Cite This: ACS Energy Lett. 2021, 6, 3244−3251

Read Online

ACCESS | Metrics & More | Article Recommendations | Supporting Information



Non-radiative recombination via defects is a major loss mechanism for nearly all photovoltaic technologies.[1] Despite their frequently quoted "defect tolerance",[2,3] halide perovskites are no exception to this rule, given that it remains difficult to exceed luminescence quantum efficiencies of a few percent at photovoltaic working conditions in devices.[4−6] Given the importance of non-radiative recombination, the experimental detection of the culprits, i.e., the most recombination-active defects, is of substantial importance for controlled optimization of devices but also for long-term strategic decisions. One such strategic decision is the assessment of possible performance benefits associated with going from polycrystalline thin films to single crystals[7,8] as active elements in perovskite solar cells. A substantial amount of experimental data[9−17] indicates that polycrystalline thin films of lead halide perovskites typically have defect densities on the order of $10^{15}$−$10^{16}$ $cm^{-3}$, while single crystals are typically reported[9,14,18−20] to have bulk defect densities of $10^{12}$ $cm^{-3}$ or lower. These findings support an intuitive rationale, namely that single crystals have orders of magnitude lower defect densities than thin films that should contain a certain density of defects at their grain boundaries. This narrative has even inspired paper titles such as the one from Brenes et al.,[21] who write about "Metal Halide Perovskite Polycrystalline Films Exhibiting Properties of Single Crystals" while reporting exceptionally long charge-carrier lifetimes in perovskite thin films.

When we inspect the available evidence for these substantial differences between single-crystal and thin-film defect densities further, we note that the defect densities are typically measured with two dominant techniques, namely (i) a range of capacitance-based methods[9,22] and (ii) observations of the trap-filled limit in single-carrier devices.[23] These two methods are complemented with a range of other techniques where insufficient data exists to make systematic meta-analyses comparing thin films with single crystals. Other techniques to measure defect densities include (iii) transient spectroscopic methods such as transient photoluminescence (tr-PL)[24] or transient photoconductivity,[17] (iv) surface physics techniques such as ultraviolet photoelectron spectroscopy[25] (UPS) or more advanced techniques such as constant final state yield spectroscopy,[26] (v) thermally stimulated current measurements,[27] and (vi) optical techniques based on subgap absorption[28,29] or emission.[30,31]

Differences between thin films and single crystals are mostly based on observations derived from the first two types of methods that share the hugely important feature that they detect defects via the amount of charge stored on these defects. For this charge to affect either the solar cell capacitance or the current of a single-carrier device, it has to affect the electrostatic potential distribution of the measured sample to a degree that the charge becomes detectable.[32] For a certain charge density per volume to affect the electrostatic potential of a device with two electrodes, this charge density has to substantially exceed the surface charge densities $\sigma$ on the two electrodes separated by the sample thickness $d$. If this was not the case, the electrostatic potential $\varphi$ would just drop linearly from one electrode to the other. Free carriers might affect the potential as in the space-charge-limited current regime in a single-carrier device, or in case of the diffusion or chemical capacitance of a diode under forward bias, but the net ionized defect density $N_{def}$ will remain invisible. From this very simple rationale, we would expect that $qN_{def}d \gg \sigma$ should hold to ensure that the ionized defect density will actually be visible in any charge-based measurement. Let us now assume that the surface charge density of the electrodes is given by the equation for a plate capacitor, i.e., $\sigma = \varepsilon_0\varepsilon_r\Delta\varphi/d$, where $\Delta\varphi$ is the electrostatic potential difference between the two electrodes. For the case of a diode, where $\Delta\varphi = V_{bi} - V$, this immediately results in the condition

$$N_{def} \gg \frac{\varepsilon_0\varepsilon_r(V_{bi} - V)}{qd^2} \tag{1}$$

where $q$ is the elementary charge, $V_{bi}$ is the built-in voltage, $V$ is the applied voltage, and $\varepsilon_0$ and $\varepsilon_r$ are the vacuum and relative permittivity. The most noteworthy feature of eq 1 is that the ionized defect density has to exceed a value that depends inversely on the layer thickness ($d$) squared. Thus, the argument that a volume density has to compete with a surface density automatically leads to the situation where higher volume charge densities are needed in thinner films to have a notable effect on the electrostatic potential. One might think that this implies that the measured defect densities in thin films

Received: July 12, 2021
Accepted: August 12, 2021

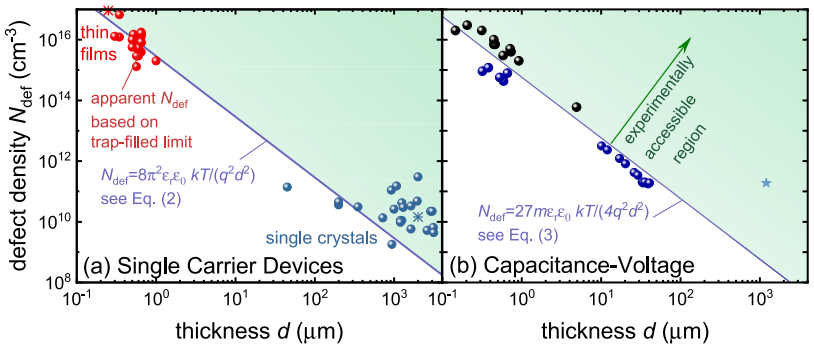


**Figure 1.** (a) Apparent defect densities derived from the trap-filled regime of *JV* curves taken from single-carrier devices based on lead halide perovskites (symbols).[11−14,18−20,37−49] In addition, two data points are added for lead-free perovskites (∗-shaped symbols).[50,51] We also show the region that should show a trap-filled current according to drift−diffusion simulations. (b) Apparent defect density from capacitance−voltage (black) and drive-level capacitance profiling (DLCP) measurements (blue) as a function of absorber thickness.[9,10,15,52−57] The lines show the minimum volume defect density that should be measurable according to eq 3. With very few exceptions (e.g., the light blue data point in (b)), the experimental data points for both methods are close to the threshold of detectability over orders of magnitude in thickness. Some of the data points in panel (b) as well as the analytical detection limit have previously been presented in refs 36 and 58.

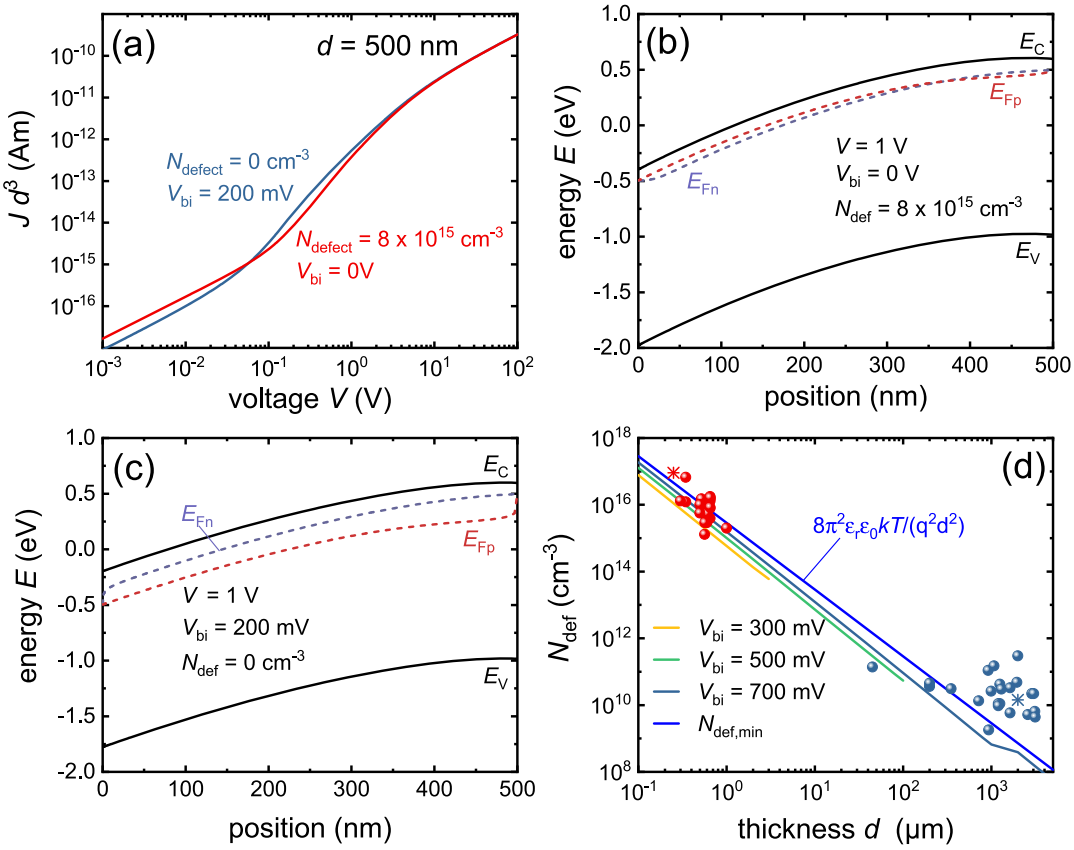


**Figure 2.** (a) Simulated *JV* curve for electron-only device with a defect density of 8 × 10$^{15}$ cm$^{-3}$ and no built-in voltage (red) compared to a defect-free device with a built-in voltage of 200 mV (blue). Note that the current density *J* has been multiplied by the thickness cubed ($d^3$). (b, c) Corresponding band diagram at $V$ = 1 V for the two cases from (a). (d) Apparent defect density for different thicknesses for devices with $V_{bi}$ > 0. The simulated lines are all parallel to the minimal detectable defect density. When a line ends, the corresponding *JV* curves will not have a slope d ln *J*/d ln $V$ > 2 at any voltage, and it is therefore unlikely that the effects of non-zero $V_{bi}$ could be mistaken for a trap-limited current regime.

are always higher than in thicker films or crystals because one would never be able to detect lower defect densities in thin films in the first place. If this was the case, there would be a bias toward reporting the seemingly obvious finding that single crystals have lower defect densities than thin films. Let us therefore have a quick look at literature data on defect densities for samples of various thicknesses, focusing on single-carrier devices (see Figure 1a) and capacitance-based methods (see Figure 1b). Both data sets show a clear trend that roughly follows eq 1. Furthermore, we highlighted in color the regions for which we should be able to reliably determine defect densities. Below the blue line (white region), the trap density is



https://doi.org/10.1021/acsenergylett.1c01449
ACS Energy Lett. 2021, 6, 3244−3251

too low to observe a trap-limited current in our simulations. We find that the experimental data lies fairly close to the threshold of detectability over many orders of magnitude of thicknesses. To describe the empirical threshold of detectability resulting from the simulations of the single-carrier devices, we find that

$$N_{\mathrm{def}} > \frac{8\pi^2 \varepsilon_0 \varepsilon_r kT}{q^2 d^2} \tag{2}$$

approximately provides the threshold above which the trap-filled current becomes visible in the simulations (cf. Figure S3). Note that the same equation (save for a factor 2) was recently mentioned by Le Corre et al.[33] to be the detection threshold for the trap-limited current. The argument of Le Corre et al.[33] was that the trap or defect density has to exceed the carrier density that would be present in the film anyway, even in a defect-free case, in order to change the electric field in the device such that the current would be affected by the presence of the charged defects.[34,35]

In Figure 1b, we use the detection threshold for detecting charge densities in capacitance−voltage measurements that we have derived recently[36] and that is given by

$$N_{\mathrm{def}} > \frac{27 m_{\mathrm{CV}} kT \varepsilon_r \varepsilon_0}{4 q^2 d^2} \tag{3}$$

where $m_{\mathrm{CV}}$ is a parameter describing the steepness of the capacitance−voltage relation at forward bias (see SI, section 3). As noted previously, the experimental data lies very close to the detectability threshold, with the exception of a single crystal measured by Ni et al.[9] (see blue star in Figure 1b) that seems to be a rare example of a justified assignment of a (bulk) defect density from a capacitance measurement. All other data shown in Figure 1b originates from cells that must have defect densities equal to or lower than the threshold. We also note that both the use of single-carrier devices and the use of capacitance−voltage measurements are limited by variants of eq 1 that all contain its basic feature, namely a proportionality to $\varepsilon_0\varepsilon_r/qd^2$ that is always multiplied with a factor of unit V that slightly differs depending on the type of measurement and the operating voltages involved in the data analysis. Furthermore, both methods are only sensitive to ionized defects, while neutral defects remain invisible. Finally, they can only detect net charge densities,[33] meaning that any equal densities of positively and negatively charged defects cancel each other out and remain invisible in these methods.

Thus, the question arises whether the data shown in Figure 1 provides any evidence for lower defect densities in perovskite single crystals. Are there credible reasons why the experimental data points all lie close to the calculated detectability limits? In the case of capacitance−voltage data, there is ample evidence that methods based on the existence of a space-charge region and the validity of the depletion approximation may easily be misinterpreted, leading to reports of apparent doping or defect densities.[36,53,59] This is a phenomenon that has been reported in perovskites but previously also in other thin-film solar cells.[59] For the analysis of the trap-filled limit in single-carrier devices, there are much fewer discussions on the detectability limits and its implications.[33] One might argue that in the absence of a sufficient net ionized defect density, the current−voltage curves should not show a trap-filled regime. Hence the fact that there is such a regime in the data should be sufficient evidence for using the determined defect densities.

The problem with this argument is illustrated in Figure 2. Ionized defects are only one of several reasons leading to an exponential increase of the current with voltage in a single-carrier measurement.[60] Figure 2a shows two current−voltage ($JV$) curves, simulated using a drift−diffusion simulation as explained in section 4 in the SI, that are very similar and show a fairly steep increase of the current density between 0.1 and 1 V. In one case (blue), this is due to a non-zero built-in voltage of 200 mV, and in the other case (red), it is due to a non-zero defect density. In both cases, a barrier exists for electrons that makes current flow difficult at low forward bias. Overcoming the electrostatic potential barrier requires an additional voltage to enable the same current flow as in a defect-free device. Figure 2b shows the band diagram at 1 V forward bias in the case of a non-zero defect density, while Figure 2c shows the band diagram for a non-zero $V_{\mathrm{bi}}$. We note that the band diagrams look fairly similar, despite the different origins of the electrostatic potential barriers. Hence, it is not surprising that the two $JV$ curves look equally similar.

The influence of injection barriers can be easily tested by comparing forward vs reverse bias $JV$ curves (see Figure S5). Even more, the difference in injection barriers can also be calculated from the comparison of forward vs reverse bias sweeps.[61] However, given that this check is hardly ever reported in the literature, we tested what would happen if we had a small, undetected built-in voltage in our samples. If we now intentionally misinterpret the feature caused by this built-in voltage $V_{\mathrm{bi}}$ as a trap-limited current, we obtain Figure 2d. We see that the apparent defect density roughly follows the same trend as the literature data. Note that the misinterpretation of $JV$ curves of samples with non-zero built-in voltages can be avoided by checking the forward bias vs reverse bias $JV$ curves of the samples.[61] Here, the key is not the scan direction as in the studies of hysteresis but the polarity of the electrodes. For non-zero built-in voltages, the forward vs reverse bias $JV$ curves will look substantially different, while they would look identical if they had zero $V_{\mathrm{bi}}$ but a non-zero density of charged defects. Unfortunately, the forward vs reverse bias branches of the $JV$ curves are only rarely[62] reported in the literature, making it impossible to exclude the effect of non-zero $V_{\mathrm{bi}}$ on the trend seen in Figure 1a.

Hence, even without considering the additional complication of ion movement,[62−64] we arrive at the conclusion that Figure 1 does not provide solid evidence for thin films having higher defect densities than single crystals. All data points for thin films are so close to the detection threshold that a safe determination of defect densities seems impossible. Figure 1 does, however, provide fairly solid evidence that at least some single crystals must have very low ($<10^{12}$ cm$^{-3}$) densities of charged defects. This is either because the data points are clearly above the detection threshold and therefore represent a sensible application of the respective method or because the lines give an upper limit for the charged defect densities for each thickness. However, there is so far no evidence for any trend in defect density with sample thickness, and—most likely—we will never be able to measure a trend as long as we rely on measuring *charge* densities. At least lead halide perovskites of good quality seem to have defect densities that are consistently lower than (or close to) the detection threshold of these methods, which is good news for the technology but bad news for the applicability of methods based on detecting changes in electrostatic potential. Note that no matter how much a data point exceeds the detection thresholds


https://doi.org/10.1021/acsenergylett.1c01449
ACS Energy Lett. 2021, 6, 3244−3251

in Figure 1, we always have to remember the caveat that defects could also be neutral or appear in pairs of positively and negatively charged defects and therefore would be invisible in any charge-based method.

Alternative methods such as photoelectron spectroscopy have fundamental limitations caused by their surface sensitivity and hence insensitivity to bulk defects. However, they show substantial potential to characterize near-surface defects as a function of energy and position, especially if photoelectron spectroscopy variations are employed that are optimized for dynamic range[26,65] or for spatial resolution.[66] Extraction of defect densities from transient methods[24] requires the defect density to be on the order of the charge-carrier density during the measurement. Otherwise, the transient will only be sensitive to the product of capture coefficients and trap densities without being able to discriminate between the two. Typical charge carrier densities during such measurements are on the order of $10^{15}$–$10^{17}$ $cm^{-3}$ and thereby substantially higher than many of the data points in Figure 1 that present upper limits of the densities of ionized defects. Thus, the reliable measurement of bulk defect densities over orders of magnitude in thickness and defect density is—unsurprisingly—a challenge not easily overcome.

What is possible, however, is to measure the *impact* of traps on recombination via the lifetime of charge carriers.[67,68] Eventually, the lifetime or the recombination coefficients will control the open-circuit voltage of a device.[69] The actual defect density may not be such a good figure of merit in the first place if we consider how large variations of capture coefficients can be. A recent theoretical paper from Zhang et al.[70] calculated capture coefficients of certain hydrogen vacancies to be on the order of $10^{-4}$ $cm^3/s$, i.e., an extremely high value. This implies that, for a bulk lifetime target of $\tau > 1$ $\mu s$, one needs defect densities $N_{def} < (10^{-6} \times 10^{-4}\ cm^3)^{-1} = 10^{10}\ cm^{-3}$, which would become detectable only at a thickness of millimeters. Thus, if these types of hydrogen vacancies are actually the decisive defect species, it might be very difficult to directly measure those defects, while the indirect measurement of material and surface quality via the variation of carrier lifetimes is fairly straightforward.

In order to check for any thickness-dependent trend in the impact of traps on recombination, Figure 3 shows the comparison of lifetime data from literature derived from transient photoluminescence and transient microwave photoconductivity (TRMC) measurements as a function of sample thickness. Given that, in high-level injection, the photoluminescence signal is proportional to $n^2$ and the conductivity to $n$, where $n$ is the carrier density, we divided the TRMC lifetime by a factor 2 to stay comparable with photoluminescence. We note that there is so far no clear trend to be seen. In the case of thin films and single crystals, surface recombination is likely to have a substantial impact not only on the $V_{oc}$ of a solar cell but also on the lifetime measured by transient methods. One way to reduce the impact of the surface is to measure transient photoluminescence using two-photon absorption, which is, however, only rarely reported in the literature. We note that there is two-photon absorption data on single crystals with a 70 $\mu s$ lifetime, which indicates that single crystals can indeed have excellent bulk properties that have not been achieved so far with thin films.

Based on the data shown above, we arrive at several conclusions and suggestions to the community: Charge densities can only be safely measured if they are above the detection limits given in Figure 1 and eqs 2 and 3. Given that all thin-film data is close to the detection threshold, we currently have no information based on single-carrier devices or capacitance methods that would provide a reliable value of the density of charged defects in thin-film perovskite devices. Whether there is a significant difference between the defect densities of single crystals and thin films we therefore cannot say using the data in Figure 1.

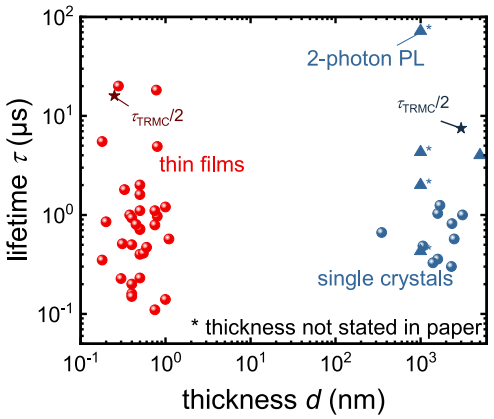


**Figure 3. Lifetimes measured using transient PL (lighter spheres), two-photon transient PL (triangles), and transient microwave photoconductivity (star) on lead halide perovskite films (red) and crystals (blue). Data was extracted from refs 19, 21, 39, 42, 43, 45, 48, 67, 71–96. In order to enable a fair comparison between data obtained from PL ~ $n^2$ and TRMC ~ $n$, we divided the TRMC lifetimes by a factor 2. So far, the highest lifetime is from a single crystal, but there is no substantial difference between the typical values of thin films and single crystals. Note that for some of the single crystal data, no thickness was specified in the paper. In order to still be able to include the data, we set the thickness arbitrarily to 1 mm.**

If defect densities are reported that are based on the measurement of charge densities, the data could easily be compared with eqs 2 and 3. If the defect density is substantially above the detection threshold, the data can be safely published. If the defect density is below or close to the detection threshold, the data should be reported as an upper limit to the density of charged defects. In the case of *JV* curves of single-carrier devices, we suggest to always publish forward and reverse voltage data to check for asymmetric injection barriers and minimize the risk of wrongly assigning a defect density to a feature of the current–voltage curve that is caused by a non-zero built-in voltage.[61]

**Johanna Siekmann**
**Sandheep Ravishankar**
**Thomas Kirchartz** orcid.org/0000-0002-6954-8213

## ■ ASSOCIATED CONTENT

### Supporting Information

The Supporting Information is available free of charge at https://pubs.acs.org/doi/10.1021/acsenergylett.1c01449.

Discussions of Debye length, trap filled limit in single-carrier devices, $m_{cv}$ factor, and drift-diffusion simulations, including Figures S1–S9 (PDF)

## ■ AUTHOR INFORMATION

Complete contact information is available at: https://pubs.acs.org/10.1021/acsenergylett.1c01449



https://doi.org/10.1021/acsenergylett.1c01449
ACS Energy Lett. 2021, 6, 3244–3251

## Notes

Views expressed in this Viewpoint are those of the authors and not necessarily the views of the ACS.
The authors declare no competing financial interest.

## ■ ACKNOWLEDGMENTS

The authors acknowledge funding from the Helmholtz Association via the program oriented funding scheme (POF IV).

## ■ REFERENCES

(1) Green, M. A.; Ho-Baillie, A. W. Y. Pushing to the Limit: Radiative Efficiencies of Recent Mainstream and Emerging Solar Cells. *ACS Energy Lett.* **2019**, *4*, 1639−1644.
(2) Brandt, R. E.; Poindexter, J. R.; Gorai, P.; Kurchin, R. C.; Hoye, R. L. Z.; Nienhaus, L.; Wilson, M. W. B.; Polizzotti, J. A.; Sereika, R.; Zaltauskas, R.; Lee, L. C.; MacManus-Driscoll, J. L.; Bawendi, M.; Stevanoviç, V.; Buonassisi, T. Searching for Defect-Tolerant Photovoltaic Materials: Combined Theoretical and Experimental Screening. *Chem. Mater.* **2017**, *29* (11), 4667−4674.
(3) Brandt, R. E.; Stevanoviç, V.; Ginley, D. S.; Buonassisi, T. Identifying defect-tolerant semiconductors with high minority-carrier lifetimes: beyond hybrid lead halide perovskites. *MRS Commun.* **2015**, *5* (02), 265−275.
(4) Liu, Z.; Siekmann, J.; Klingebiel, B.; Rau, U.; Kirchartz, T. Interface Optimization via Fullerene Blends Enables Open-Circuit Voltages of 1.35 V in $CH_3NH_3Pb(I_{0.8}Br_{0.2})_3$ Solar Cells. *Adv. Energy Mater.* **2021**, *11*, 2003386.
(5) Yoo, J. J.; Seo, G.; Chua, M. R.; Park, T. G.; Lu, Y.; Rotermund, F.; Kim, Y.-K.; Moon, C. S.; Jeon, N. J.; Correa-Baena, J.-P.; Bulović, V.; Shin, S. S.; Bawendi, M. G.; Seo, J. Efficient perovskite solar cells via improved carrier management. *Nature* **2021**, *590* (7847), 587−593.
(6) Jeong, J.; Kim, M.; Seo, J.; Lu, H.; Ahlawat, P.; Mishra, A.; Yang, Y.; Hope, M. A.; Eickemeyer, F. T.; Kim, M.; Yoon, Y. J.; Choi, I. W.; Darwich, B. P.; Choi, S. J.; Jo, Y.; Lee, J. H.; Walker, B.; Zakeeruddin, S. M.; Emsley, L.; Rothlisberger, U.; Hagfeldt, A.; Kim, D. S.; Grätzel, M.; Kim, J. Y. Pseudo-halide anion engineering for $\alpha$-$FAPbI_3$ perovskite solar cells. *Nature* **2021**, *592* (7854), 381−385.
(7) Chen, Z.; Turedi, B.; Alsalloum, A. Y.; Yang, C.; Zheng, X.; Gereige, I.; AlSaggaf, A.; Mohammed, O. F.; Bakr, O. M. Single-Crystal $MAPbI_3$ Perovskite Solar Cells Exceeding 21% Power Conversion Efficiency. *ACS Energy Lett.* **2019**, *4* (6), 1258−1259.
(8) Turedi, B.; Yeddu, V.; Zheng, X.; Kim, D. Y.; Bakr, O. M.; Saidaminov, M. I. Perovskite Single-Crystal Solar Cells: Going Forward. *ACS Energy Lett.* **2021**, *6* (2), 631−642.
(9) Ni, Z.; Bao, C.; Liu, Y.; Jiang, Q.; Wu, W.-Q.; Chen, S.; Dai, X.; Chen, B.; Hartweg, B.; Yu, Z.; Holman, Z.; Huang, J. Resolving spatial and energetic distributions of trap states in metal halide perovskite solar cells. *Science* **2020**, *367* (6484), 1352−1358.
(10) Futscher, M. H.; Gangishetty, M. K.; Congreve, D. N.; Ehrler, B. Quantifying mobile ions and electronic defects in perovskite-based devices with temperature-dependent capacitance measurements: Frequency vs time domain. *J. Chem. Phys.* **2020**, *152* (4), 044202.
(11) Son, D.-Y.; Kim, S.-G.; Seo, J.-Y.; Lee, S.-H.; Shin, H.; Lee, D.; Park, N.-G. Universal Approach toward Hysteresis-Free Perovskite Solar Cell via Defect Engineering. *J. Am. Chem. Soc.* **2018**, *140* (4), 1358−1364.
(12) Jiang, L.-L.; Wang, Z.-K.; Li, M.; Zhang, C.-C.; Ye, Q.-Q.; Hu, K.-H.; Lu, D.-Z.; Fang, P.-F.; Liao, L.-S. Passivated Perovskite Crystallization via g-$C_3N_4$ for High-Performance Solar Cells. *Adv. Funct. Mater.* **2018**, *28* (7), 1705875.
(13) Wu, Y.; He, Y.; Li, S.; Li, X.; Liu, Y.; Sun, Q.; Cui, Y.; Hao, Y.; Wu, Y. Efficient inverted perovskite solar cells with preferential orientation and suppressed defects of methylammonium lead iodide by introduction of phenothiazine as additive. *J. Alloys Compd.* **2020**, *823*, 153717.
(14) Dong, Q.; Fang, Y.; Shao, Y.; Mulligan, P.; Qiu, J.; Cao, L.; Huang, J. Electron-hole diffusion lengths > 175 $\mu$m in solution-grown $CH_3NH_3PbI_3$ single crystals. *Science* **2015**, *347* (6225), 967.
(15) Zohar, A.; Kulbak, M.; Levine, I.; Hodes, G.; Kahn, A.; Cahen, D. What limits the open-circuit voltage of bromide perovskite-based solar cells? *ACS Energy Lett.* **2019**, *4* (1), 1−7.
(16) Duan, H. S.; Zhou, H.; Chen, Q.; Sun, P.; Luo, S.; Song, T. B.; Bob, B.; Yang, Y. The identification and characterization of defect states in hybrid organic-inorganic perovskite photovoltaics. *Phys. Chem. Chem. Phys.* **2015**, *17* (1), 112−116.
(17) Hutter, E. M.; Eperon, G. E.; Stranks, S. D.; Savenije, T. J. Charge Carriers in Planar and Meso-Structured Organic−Inorganic Perovskites: Mobilities, Lifetimes, and Concentrations of Trap States. *J. Phys. Chem. Lett.* **2015**, *6* (15), 3082−3090.
(18) Adinolfi, V.; Yuan, M.; Comin, R.; Thibau, E. S.; Shi, D.; Saidaminov, M. I.; Kanjanaboos, P.; Kopilovic, D.; Hoogland, S.; Lu, Z.-H.; Bakr, O. M.; Sargent, E. H. The In-Gap Electronic State Spectrum of Methylammonium Lead Iodide Single-Crystal Perovskites. *Adv. Mater.* **2016**, *28* (17), 3406−3410.
(19) Shi, D.; Adinolfi, V.; Comin, R.; Yuan, M.; Alarousu, E.; Buin, A.; Chen, Y.; Hoogland, S.; Rothenberger, A.; Katsiev, K.; Losovyj, Y.; Zhang, X.; Dowben, P. A.; Mohammed, O. F.; Sargent, E. H.; Bakr, O. M. Low trap-state density and long carrier diffusion in organolead trihalide perovskite single crystals. *Science* **2015**, *347* (6221), 519−522.
(20) Liu, Y.; Zhang, Y.; Zhao, K.; Yang, Z.; Feng, J.; Zhang, X.; Wang, K.; Meng, L.; Ye, H.; Liu, M.; Liu, S. A 1300 $mm^2$ Ultrahigh-Performance Digital Imaging Assembly using High-Quality Perovskite Single Crystals. *Adv. Mater.* **2018**, *30* (29), 1707314.
(21) Brenes, R.; Guo, D.; Osherov, A.; Noel, N. K.; Eames, C.; Hutter, E. M.; Pathak, S. K.; Niroui, F.; Friend, R. H.; Islam, M. S.; Snaith, H. J.; Buloviç, V.; Savenije, T. J.; Stranks, S. D. Metal Halide Perovskite Polycrystalline Films Exhibiting Properties of Single Crystals. *Joule* **2017**, *1* (1), 155−167.
(22) Heath, J.; Zabierowski, P., Capacitance Spectroscopy of Thin-Film Solar Cells. In *Advanced Characterization Techniques for Thin Film Solar Cells*; Abou-Ras, D., Kirchartz, T., Rau, U., Eds.; Wiley-VCH: Weinheim, 2011; pp 81−105.
(23) Lampert, M. A. Volume-controlled current injection in insulators. *Rep. Prog. Phys.* **1964**, *27* (1), 329.
(24) Stranks, S. D.; Burlakov, V. M.; Leijtens, T.; Ball, J. M.; Goriely, A.; Snaith, H. J. Recombination Kinetics in Organic-Inorganic Perovskites: Excitons, Free Charge, and Subgap States. *Phys. Rev. Appl.* **2014**, *2* (3), 034007.
(25) Zhang, F.; Hamill, J. C., Jr.; Loo, Y.-L.; Kahn, A. Gap States in Methylammonium Lead Halides: The Link to Dimethylsulfoxide? *Adv. Mater.* **2020**, *32* (42), 2003482.
(26) Levine, I.; Shimizu, K.; Lomuscio, A.; Kulbak, M.; Rehermann, C.; Zohar, A.; Abdi-Jalebi, M.; Zhao, B.; Siebentritt, S.; Zu, F.; Koch, N.; Kahn, A.; Hodes, G.; Friend, R. H.; Ishii, H.; Cahen, D. Direct Probing of Gap States and Their Passivation in Halide Perovskites by High-Sensitivity, Variable Energy Ultraviolet Photoelectron Spectroscopy. *J. Phys. Chem. C* **2021**, *125* (9), 5217−5225.
(27) Baumann, A.; Väth, S.; Rieder, P.; Heiber, M. C.; Tvingstedt, K.; Dyakonov, V. Identification of Trap States in Perovskite Solar Cells. *J. Phys. Chem. Lett.* **2015**, *6*, 2350−2354.
(28) Holovský, J.; Peter Amalathas, A.; Landová, L.; Dzurňák, B.; Conrad, B.; Ledinský, M.; Hájková, Z.; Pop-Georgievski, O.; Svoboda, J.; Yang, T. C.-J.; Jeangros, Q. Lead Halide Residue as a Source of Light-Induced Reversible Defects in Hybrid Perovskite Layers and Solar Cells. *ACS Energy Lett.* **2019**, *4* (12), 3011−3017.
(29) Wu, S.; Zhang, J.; Li, Z.; Liu, D.; Qin, M.; Cheung, S. H.; Lu, X.; Lei, D.; So, S. K.; Zhu, Z.; Jen, A. K. Y. Modulation of Defects and Interfaces through Alkylammonium Interlayer for Efficient Inverted Perovskite Solar Cells. *Joule* **2020**, *4* (6), 1248−1262.
(30) Meggiolaro, D.; Motti, S. G.; Mosconi, E.; Barker, A. J.; Ball, J.; Andrea Riccardo Perini, C.; Deschler, F.; Petrozza, A.; De Angelis, F. Iodine chemistry determines the defect tolerance of lead-halide perovskites. *Energy Environ. Sci.* **2018**, *11* (3), 702−713.


https://doi.org/10.1021/acsenergylett.1c01449
*ACS Energy Lett.* 2021, 6, 3244−3251

(31) Motti, S. G.; Meggiolaro, D.; Martani, S.; Sorrentino, R.; Barker, A. J.; De Angelis, F.; Petrozza, A. Defect Activity in Lead Halide Perovskites. *Adv. Mater.* **2019**, *31* (47), 1901183.
(32) Kirchartz, T.; Cahen, D. Minimum doping densities for p−n junctions. *Nature Energy* **2020**, *5* (12), 973−975.
(33) Le Corre, V. M.; Duijnstee, E. A.; El Tambouli, O.; Ball, J. M.; Snaith, H. J.; Lim, J.; Koster, L. J. A. Revealing Charge Carrier Mobility and Defect Densities in Metal Halide Perovskites via Space-Charge-Limited Current Measurements. *ACS Energy Lett.* **2021**, *6* (3), 1087−1094.
(34) Röhr, J. A.; Kirchartz, T.; Nelson, J. On the correct interpretation of the low voltage regime in intrinsic single-carrier devices. *J. Phys.: Condens. Matter* **2017**, *29* (20), 205901.
(35) Wetzelaer, G. A. H.; Blom, P. W. M. Ohmic current in organic metal-insulator-metal diodes revisited. *Phys. Rev. B: Condens. Matter Mater. Phys.* **2014**, *89* (24), 241201.
(36) Ravishankar, S.; Unold, T.; Kirchartz, T. Comment on "Resolving spatial and energetic distributions of trap states in metal halide perovskite solar cells. *Science* **2021**, *371* (6532), eabd8014.
(37) Bu, T.; Liu, X.; Zhou, Y.; Yi, J.; Huang, X.; Luo, L.; Xiao, J.; Ku, Z.; Peng, Y.; Huang, F.; Cheng, Y.-B.; Zhong, J. A novel quadruple-cation absorber for universal hysteresis elimination for high efficiency and stable perovskite solar cells. *Energy Environ. Sci.* **2017**, *10* (12), 2509−2515.
(38) Guo, Y.; Ma, J.; Lei, H.; Yao, F.; Li, B.; Xiong, L.; Fang, G. Enhanced performance of perovskite solar cells via anti-solvent nonfullerene Lewis base IT-4F induced trap-passivation. *J. Mater. Chem. A* **2018**, *6* (14), 5919−5925.
(39) Han, Q.; Bae, S.-H.; Sun, P.; Hsieh, Y.-T.; Yang, Y.; Rim, Y. S.; Zhao, H.; Chen, Q.; Shi, W.; Li, G.; Yang, Y. Single Crystal Formamidinium Lead Iodide (FAPbI3): Insight into the Structural, Optical, and Electrical Properties. *Adv. Mater.* **2016**, *28* (11), 2253−2258.
(40) Liu, Y.; Sun, J.; Yang, Z.; Yang, D.; Ren, X.; Xu, H.; Yang, Z.; Liu, S. 20-mm-Large Single-Crystalline Formamidinium-Perovskite Wafer for Mass Production of Integrated Photodetectors. *Adv. Opt. Mater.* **2016**, *4* (11), 1829−1837.
(41) Liu, Y.; Yang, Z.; Cui, D.; Ren, X.; Sun, J.; Liu, X.; Zhang, J.; Wei, Q.; Fan, H.; Yu, F.; Zhang, X.; Zhao, C.; Liu, S. Two-Inch-Sized Perovskite $CH_3NH_3PbX_3$ (X = Cl, Br, I) Crystals: Growth and Characterization. *Adv. Mater.* **2015**, *27* (35), 5176−5183.
(42) Maculan, G.; Sheikh, A. D.; Abdelhady, A. L.; Saidaminov, M. I.; Haque, M. A.; Murali, B.; Alarousu, E.; Mohammed, O. F.; Wu, T.; Bakr, O. M. $CH_3NH_3PbCl_3$ Single Crystals: Inverse Temperature Crystallization and Visible-Blind UV-Photodetector. *J. Phys. Chem. Lett.* **2015**, *6* (19), 3781−3786.
(43) Min, H.; Kim, M.; Lee, S.-U.; Kim, H.; Kim, G.; Choi, K.; Lee, J. H.; Seok, S. I. Efficient, stable solar cells by using inherent bandgap of $\alpha$-phase formamidinium lead iodide. *Science* **2019**, *366* (6466), 749−753.
(44) Saidaminov, M. I.; Haque, M. A.; Almutlaq, J.; Sarmah, S.; Miao, X.-H.; Begum, R.; Zhumekenov, A. A.; Dursun, I.; Cho, N.; Murali, B.; Mohammed, O. F.; Wu, T.; Bakr, O. M. Inorganic Lead Halide Perovskite Single Crystals: Phase-Selective Low-Temperature Growth, Carrier Transport Properties, and Self-Powered Photodetection. *Adv. Opt. Mater.* **2017**, *5* (2), 1600704.
(45) Tan, H.; Jain, A.; Voznyy, O.; Lan, X.; García de Arquer, F. P.; Fan, J. Z.; Quintero-Bermudez, R.; Yuan, M.; Zhang, B.; Zhao, Y.; Fan, F.; Li, P.; Quan, L. N.; Zhao, Y.; Lu, Z.-H.; Yang, Z.; Hoogland, S.; Sargent, E. H. Efficient and stable solution-processed planar perovskite solar cells via contact passivation. *Science* **2017**, *355* (6326), 722−726.
(46) Xiang, T.; Zhang, Y.; Wu, H.; Li, J.; Yang, L.; Wang, K.; Xia, J.; Deng, Z.; Xiao, J.; Li, W.; Ku, Z.; Huang, F.; Zhong, J.; Peng, Y.; Cheng, Y.-B. Universal defects elimination for high performance thermally evaporated $CsPbBr_3$ perovskite solar cells. *Sol. Energy Mater. Sol. Cells* **2020**, *206*, 110317.
(47) Yang, D.; Zhou, X.; Yang, R.; Yang, Z.; Yu, W.; Wang, X.; Li, C.; Liu, S.; Chang, R. P. H. Surface optimization to eliminate hysteresis for record efficiency planar perovskite solar cells. *Energy Environ. Sci.* **2016**, *9* (10), 3071−3078.
(48) Yao, F.; Peng, J.; Li, R.; Li, W.; Gui, P.; Li, B.; Liu, C.; Tao, C.; Lin, Q.; Fang, G. Room-temperature liquid diffused separation induced crystallization for high-quality perovskite single crystals. *Nat. Commun.* **2020**, *11* (1), 1194.
(49) Zhumekenov, A. A.; Saidaminov, M. I.; Haque, M. A.; Alarousu, E.; Sarmah, S. P.; Murali, B.; Dursun, I.; Miao, X.-H.; Abdelhady, A. L.; Wu, T.; Mohammed, O. F.; Bakr, O. M. Formamidinium Lead Halide Perovskite Crystals with Unprecedented Long Carrier Dynamics and Diffusion Length. *ACS Energy Lett.* **2016**, *1* (1), 32−37.
(50) Gao, W.; Ran, C.; Xi, J.; Jiao, B.; Zhang, W.; Wu, M.; Hou, X.; Wu, Z. High-Quality $Cs_2AgBiBr_6$ Double Perovskite Film for Lead-Free Inverted Planar Heterojunction Solar Cells with 2.2% Efficiency. *ChemPhysChem* **2018**, *19* (14), 1696−1700.
(51) Zhang, Z.; Chung, C.-C.; Huang, Z.; Vetter, E.; Seyitliyev, D.; Sun, D.; Gundogdu, K.; Castellano, F. N.; Danilov, E. O.; Yang, G. Towards radiation detection using $Cs_2AgBiBr_6$ double perovskite single crystals. *Mater. Lett.* **2020**, *269*, 127667.
(52) Fischer, M.; Tvingstedt, K.; Baumann, A.; Dyakonov, V. Doping profile in planar hybrid perovskite solar cells identifying mobile ions. *ACS Applied Energy Mater.* **2018**, *1* (10), 5129−5134.
(53) Almora, O.; Aranda, C.; Mas-Marzá, E.; Garcia-Belmonte, G. On Mott-Schottky analysis interpretation of capacitance measurements in organometal perovskite solar cells. *Appl. Phys. Lett.* **2016**, *109* (17), 173903.
(54) Reichert, S.; Flemming, J.; An, Q.; Vaynzof, Y.; Pietschmann, J.-F.; Deibel, C. Ionic-Defect Distribution Revealed by Improved Evaluation of Deep-Level Transient Spectroscopy on Perovskite Solar Cells. *Phys. Rev. Appl.* **2020**, *13* (3), 034018.
(55) Subhani, W. S.; Wang, K.; Du, M.; Wang, X.; Liu, S. Interface-modification-induced gradient energy band for highly efficient CsPbIBr2 perovskite solar cells. *Adv. Energy Mater.* **2019**, *9* (21), 1803785.
(56) McGovern, L.; Koschany, I.; Grimaldi, G.; Muscarella, L. A.; Ehrler, B. Grain Size Influences Activation Energy and Migration Pathways in $MAPbBr_3$ Perovskite Solar Cells. *J. Phys. Chem. Lett.* **2021**, *12*, 2423−2428.
(57) Peng, W.; Wang, L.; Murali, B.; Ho, K.-T.; Bera, A.; Cho, N.; Kang, C.-F.; Burlakov, V. M.; Pan, J.; Sinatra, L.; Ma, C.; Xu, W.; Shi, D.; Alarousu, E.; Goriely, A.; He, J.-H.; Mohammed, O. F.; Wu, T.; Bakr, O. M. Solution-Grown Monocrystalline Hybrid Perovskite Films for Hole-Transporter-Free Solar Cells. *Adv. Mater.* **2016**, *28* (17), 3383−3390.
(58) Ravishankar, S.; Liu, Z.; Kirchartz, T. Multilayer Capacitances: How Selective Contacts Affect Capacitance Measurements of Perovskite Solar Cells. *arXiv Prepr.* **2021**, No. arXiv:2106.05758[-physics.app-ph].
(59) Kirchartz, T.; Gong, W.; Hawks, S. A.; Agostinelli, T.; MacKenzie, R. C. I.; Yang, Y.; Nelson, J. Sensitivity of the Mott-Schottky Analysis in Organic Solar Cells. *J. Phys. Chem. C* **2012**, *116* (14), 7672−7680.
(60) Kirchartz, T. Influence of diffusion on space charge limited current measurements in organic semiconductors. *Beilstein J. Nanotechnol.* **2013**, *4*, 180−188.
(61) Röhr, J. A. Direct Determination of Built-in Voltages in Asymmetric Single-Carrier Devices. *Phys. Rev. Appl.* **2019**, *11* (5), 054079.
(62) Sajedi Alvar, M.; Blom, P. W. M.; Wetzelaer, G.-J. A. H. Space-charge-limited electron and hole currents in hybrid organic-inorganic perovskites. *Nat. Commun.* **2020**, *11* (1), 4023.
(63) Moia, D.; Gelmetti, I.; Calado, P.; Fisher, W.; Stringer, M.; Game, O.; Hu, Y.; Docampo, P.; Lidzey, D.; Palomares, E.; Nelson, J.; Barnes, P. R. F. Ionic-to-electronic current amplification in hybrid perovskite solar cells: ionically gated transistor-interface circuit model explains hysteresis and impedance of mixed conducting devices. *Energy Environ. Sci.* **2019**, *12* (4), 1296−1308.

(64) Moia, D.; Maier, J. Ion Transport, Defect Chemistry, and the Device Physics of Hybrid Perovskite Solar Cells. *ACS Energy Lett.* **2021**, *6* (4), 1566−1576.
(65) Aljishi, S.; Cohen, J. D.; Jin, S.; Ley, L. Band tails in hydrogenated amorphous silicon and silicon-germanium alloys. *Phys. Rev. Lett.* **1990**, *64* (23), 2811−2814.
(66) Doherty, T. A. S.; Winchester, A. J.; Macpherson, S.; Johnstone, D. N.; Pareek, V.; Tennyson, E. M.; Kosar, S.; Kosasih, F. U.; Anaya, M.; Abdi-Jalebi, M.; Andaji-Garmaroudi, Z.; Wong, E. L.; Madéo, J.; Chiang, Y.-H.; Park, J.-S.; Jung, Y.-K.; Petoukhoff, C. E.; Divitini, G.; Man, M. K. L.; Ducati, C.; Walsh, A.; Midgley, P. A.; Dani, K. M.; Stranks, S. D. Performance-limiting nanoscale trap clusters at grain junctions in halide perovskites. *Nature* **2020**, *580* (7803), 360−366.
(67) Krückemeier, L.; Krogmeier, B.; Liu, Z.; Rau, U.; Kirchartz, T. Understanding Transient Photoluminescence in Halide Perovskite Layer Stacks and Solar Cells. *Adv. Energy Mater.* **2021**, *11*, 2003489.
(68) Kiligaridis, A.; Frantsuzov, P. A.; Yangui, A.; Seth, S.; Li, J.; An, Q.; Vaynzof, Y.; Scheblykin, I. G. Are Shockley-Read-Hall and ABC models valid for lead halide perovskites? *Nat. Commun.* **2021**, *12* (1), 3329.
(69) Kirchartz, T.; Márquez, J. A.; Stolterfoht, M.; Unold, T. Photoluminescence-Based Characterization of Halide Perovskites for Photovoltaics. *Adv. Energy Mater.* **2020**, *10* (26), 1904134.
(70) Zhang, X.; Shen, J.-X.; Turiansky, M. E.; Van de Walle, C. G. Minimizing hydrogen vacancies to enable highly efficient hybrid perovskites. *Nat. Mater.* **2021**, *20*, 971.
(71) Abdi-Jalebi, M.; Andaji-Garmaroudi, Z.; Cacovich, S.; Stavrakas, C.; Philippe, B.; Richter, J. M.; Alsari, M.; Booker, E. P.; Hutter, E. M.; Pearson, A. J.; Lilliu, S.; Savenije, T. J.; Rensmo, H.; Divitini, G.; Ducati, C.; Friend, R. H.; Stranks, S. D. Maximizing and stabilizing luminescence from halide perovskites with potassium passivation. *Nature* **2018**, *555* (7697), 497−501.
(72) Abdi-Jalebi, M.; Ibrahim Dar, M.; Senanayak, S. P.; Sadhanala, A.; Andaji-Garmaroudi, Z.; Pazos-Outón, L. M.; Richter, J. M.; Pearson, A. J.; Sirringhaus, H.; Grätzel, M.; Friend, R. H. Charge extraction via graded doping of hole transport layers gives highly luminescent and stable metal halide perovskite devices. *Science Advances* **2019**, *5* (2), eaav2012.
(73) Abdi-Jalebi, M.; Pazoki, M.; Philippe, B.; Dar, M. I.; Alsari, M.; Sadhanala, A.; Divitini, G.; Imani, R.; Lilliu, S.; Kullgren, J.; Rensmo, H.; Grätzel, M.; Friend, R. H. Dedoping of Lead Halide Perovskites Incorporating Monovalent Cations. *ACS Nano* **2018**, *12* (7), 7301−7311.
(74) Al-Ashouri, A.; Magomedov, A.; Roß, M.; Jošt, M.; Talaikis, M.; Chistiakova, G.; Bertram, T.; Márquez, J. A.; Köhnen, E.; Kasparavičius, E.; Levcenco, S.; Gil-Escrig, L.; Hages, C. J.; Schlatmann, R.; Rech, B.; Malinauskas, T.; Unold, T.; Kaufmann, C. A.; Korte, L.; Niaura, G.; Getautis, V.; Albrecht, S. Conformal monolayer contacts with lossless interfaces for perovskite single junction and monolithic tandem solar cells. *Energy Environ. Sci.* **2019**, *12* (11), 3356−3369.
(75) Bi, Y.; Hutter, E. M.; Fang, Y.; Dong, Q.; Huang, J.; Savenije, T. J. Charge Carrier Lifetimes Exceeding 15 μs in Methylammonium Lead Iodide Single Crystals. *J. Phys. Chem. Lett.* **2016**, *7* (5), 923−928.
(76) Braly, I. L.; deQuilettes, D. W.; Pazos-Outón, L. M.; Burke, S.; Ziffer, M. E.; Ginger, D. S.; Hillhouse, H. W. Hybrid perovskite films approaching the radiative limit with over 90% photoluminescence quantum efficiency. *Nat. Photonics* **2018**, *12* (6), 355−361.
(77) Caprioglio, P.; Zu, F.; Wolff, C. M.; Márquez Prieto, J. A.; Stolterfoht, M.; Becker, P.; Koch, N.; Unold, T.; Rech, B.; Albrecht, S.; Neher, D. High open circuit voltages in pin-type perovskite solar cells through strontium addition. *Sustainable Energy & Fuels* **2019**, *3* (2), 550−563.
(78) deQuilettes, D. W.; Koch, S.; Burke, S.; Paranji, R. K.; Shropshire, A. J.; Ziffer, M. E.; Ginger, D. S. Photoluminescence Lifetimes Exceeding 8 μs and Quantum Yields Exceeding 30% in Hybrid Perovskite Thin Films by Ligand Passivation. *ACS Energy Lett.* **2016**, *1* (2), 438−444.
(79) Gutierrez-Partida, E.; Hempel, H.; Caicedo-Dávila, S.; Raoufi, M.; Peña-Camargo, F.; Grischek, M.; Gunder, R.; Diekmann, J.; Caprioglio, P.; Brinkmann, K. O.; Köbler, H.; Albrecht, S.; Riedl, T.; Abate, A.; Abou-Ras, D.; Unold, T.; Neher, D.; Stolterfoht, M. Large-Grain Double Cation Perovskites with 18 μs Lifetime and High Luminescence Yield for Efficient Inverted Perovskite Solar Cells. *ACS Energy Lett.* **2021**, *6* (3), 1045−1054.
(80) Hou, Y.; Aydin, E.; De Bastiani, M.; Xiao, C.; Isikgor, F. H.; Xue, D.-J.; Chen, B.; Chen, H.; Bahrami, B.; Chowdhury, A. H.; Johnston, A.; Baek, S.-W.; Huang, Z.; Wei, M.; Dong, Y.; Troughton, J.; Jalmood, R.; Mirabelli, A. J.; Allen, T. G.; Van Kerschaver, E.; Saidaminov, M. I.; Baran, D.; Qiao, Q.; Zhu, K.; De Wolf, S.; Sargent, E. H. Efficient tandem solar cells with solution-processed perovskite on textured crystalline silicon. *Science* **2020**, *367* (6482), 1135−1140.
(81) Jeon, N. J.; Na, H.; Jung, E. H.; Yang, T.-Y.; Lee, Y. G.; Kim, G.; Shin, H.-W.; Il Seok, S.; Lee, J.; Seo, J. A fluorene-terminated hole-transporting material for highly efficient and stable perovskite solar cells. *Nature Energy* **2018**, *3* (8), 682−689.
(82) Jiang, Q.; Zhao, Y.; Zhang, X.; Yang, X.; Chen, Y.; Chu, Z.; Ye, Q.; Li, X.; Yin, Z.; You, J. Surface passivation of perovskite film for efficient solar cells. *Nat. Photonics* **2019**, *13* (7), 460−466.
(83) Kim, M.; Kim, G.-H.; Lee, T. K.; Choi, I. W.; Choi, H. W.; Jo, Y.; Yoon, Y. J.; Kim, J. W.; Lee, J.; Huh, D.; Lee, H.; Kwak, S. K.; Kim, J. Y.; Kim, D. S. Methylammonium Chloride Induces Intermediate Phase Stabilization for Efficient Perovskite Solar Cells. *Joule* **2019**, *3* (9), 2179−2192.
(84) Liu, Y.; Zhang, Y.; Yang, Z.; Feng, J.; Xu, Z.; Li, Q.; Hu, M.; Ye, H.; Zhang, X.; Liu, M.; Zhao, K.; Liu, S. Low-temperature-gradient crystallization for multi-inch high-quality perovskite single crystals for record performance photodetectors. *Mater. Today* **2019**, *22*, 67−75.
(85) Liu, Z.; Krückemeier, L.; Krogmeier, B.; Klingebiel, B.; Márquez, J. A.; Levcenko, S.; Öz, S.; Mathur, S.; Rau, U.; Unold, T.; Kirchartz, T. Open-Circuit Voltages Exceeding 1.26 V in Planar Methylammonium Lead Iodide Perovskite Solar Cells. *ACS Energy Lett.* **2019**, *4* (1), 110−117.
(86) Richter, J. M.; Abdi-Jalebi, M.; Sadhanala, A.; Tabachnyk, M.; Rivett, J. P. H.; Pazos-Outón, L. M.; Gödel, K. C.; Price, M.; Deschler, F.; Friend, R. H. Enhancing photoluminescence yields in lead halide perovskites by photon recycling and light out-coupling. *Nat. Commun.* **2016**, *7* (1), 13941.
(87) Saidaminov, M. I.; Abdelhady, A. L.; Murali, B.; Alarousu, E.; Burlakov, V. M.; Peng, W.; Dursun, I.; Wang, L.; He, Y.; Maculan, G.; Goriely, A.; Wu, T.; Mohammed, O. F.; Bakr, O. M. High-quality bulk hybrid perovskite single crystals within minutes by inverse temperature crystallization. *Nat. Commun.* **2015**, *6* (1), 7586.
(88) Staub, F.; Hempel, H.; Hebig, J.-C.; Mock, J.; Paetzold, U. W.; Rau, U.; Unold, T.; Kirchartz, T. Beyond Bulk Lifetimes: Insights into Lead Halide Perovskite Films from Time-Resolved Photoluminescence. *Phys. Rev. Appl.* **2016**, *6* (4), 044017.
(89) Stolterfoht, M.; Wolff, C. M.; Márquez, J. A.; Zhang, S.; Hages, C. J.; Rothhardt, D.; Albrecht, S.; Burn, P. L.; Meredith, P.; Unold, T.; Neher, D. Visualization and suppression of interfacial recombination for high-efficiency large-area pin perovskite solar cells. *Nature Energy* **2018**, *3* (10), 847−854.
(90) Tong, J.; Song, Z.; Kim, D. H.; Chen, X.; Chen, C.; Palmstrom, A. F.; Ndione, P. F.; Reese, M. O.; Dunfield, S. P.; Reid, O. G.; Liu, J.; Zhang, F.; Harvey, S. P.; Li, Z.; Christensen, S. T.; Teeter, G.; Zhao, D.; Al-Jassim, M. M.; van Hest, M. F. A. M.; Beard, M. C.; Shaheen, S. E.; Berry, J. J.; Yan, Y.; Zhu, K. Carrier lifetimes of > 1 μs in Sn-Pb perovskites enable efficient all-perovskite tandem solar cells. *Science* **2019**, *364* (6439), 475−479.
(91) Wolff, C. M.; Canil, L.; Rehermann, C.; Ngoc Linh, N.; Zu, F.; Ralaiarisoa, M.; Caprioglio, P.; Fiedler, L.; Stolterfoht, M.; Kogikoski, S.; Bald, I.; Koch, N.; Unger, E. L.; Dittrich, T.; Abate, A.; Neher, D. Perfluorinated Self-Assembled Monolayers Enhance the Stability and Efficiency of Inverted Perovskite Solar Cells. *ACS Nano* **2020**, *14* (2), 1445−1456.
(92) Yang, W. S.; Park, B.-W.; Jung, E. H.; Jeon, N. J.; Kim, Y. C.; Lee, D. U.; Shin, S. S.; Seo, J.; Kim, E. K.; Noh, J. H.; Seok, S. I.

Iodide management in formamidinium-lead-halide–based perovskite layers for efficient solar cells. *Science* **2017**, *356* (6345), 1376–1379.
(93) Zheng, X.; Hou, Y.; Bao, C.; Yin, J.; Yuan, F.; Huang, Z.; Song, K.; Liu, J.; Troughton, J.; Gasparini, N.; Zhou, C.; Lin, Y.; Xue, D.-J.; Chen, B.; Johnston, A. K.; Wei, N.; Hedhili, M. N.; Wei, M.; Alsalloum, A. Y.; Maity, P.; Turedi, B.; Yang, C.; Baran, D.; Anthopoulos, T. D.; Han, Y.; Lu, Z.-H.; Mohammed, O. F.; Gao, F.; Sargent, E. H.; Bakr, O. M. Managing grains and interfaces via ligand anchoring enables 22.3%-efficiency inverted perovskite solar cells. *Nature Energy* **2020**, *5* (2), 131–140.
(94) Staub, F.; Anusca, I.; Lupascu, D. C.; Rau, U.; Kirchartz, T. Effect of reabsorption and photon recycling on photoluminescence spectra and transients in lead-halide perovskite crystals. *Journal of Physics: Materials* **2020**, *3* (2), 025003.
(95) Alarousu, E.; El-Zohry, A. M.; Yin, J.; Zhumekenov, A. A.; Yang, C.; Alhabshi, E.; Gereige, I.; AlSaggaf, A.; Malko, A. V.; Bakr, O. M.; Mohammed, O. F. Ultralong Radiative States in Hybrid Perovskite Crystals: Compositions for Submillimeter Diffusion Lengths. *J. Phys. Chem. Lett.* **2017**, *8* (18), 4386–4390.
(96) Yamada, Y.; Yamada, T.; Phuong, L. Q.; Maruyama, N.; Nishimura, H.; Wakamiya, A.; Murata, Y.; Kanemitsu, Y. Dynamic Optical Properties of $CH_3NH_3PbI_3$ Single Crystals As Revealed by One- and Two-Photon Excited Photoluminescence Measurements. *J. Am. Chem. Soc.* **2015**, *137* (33), 10456–10459.



https://doi.org/10.1021/acsenergylett.1c01449
*ACS Energy Lett.* 2021, 6, 3244–3251